The University of Texas at Austin
2026 NASA RASC-AL Competition
Theme 4: Lunar Technology Demonstrations Leveraging Common Infrastructure

Demonstration of Up-scalable Surface Treatment for Earth–Moon Economy (DUSTEE)

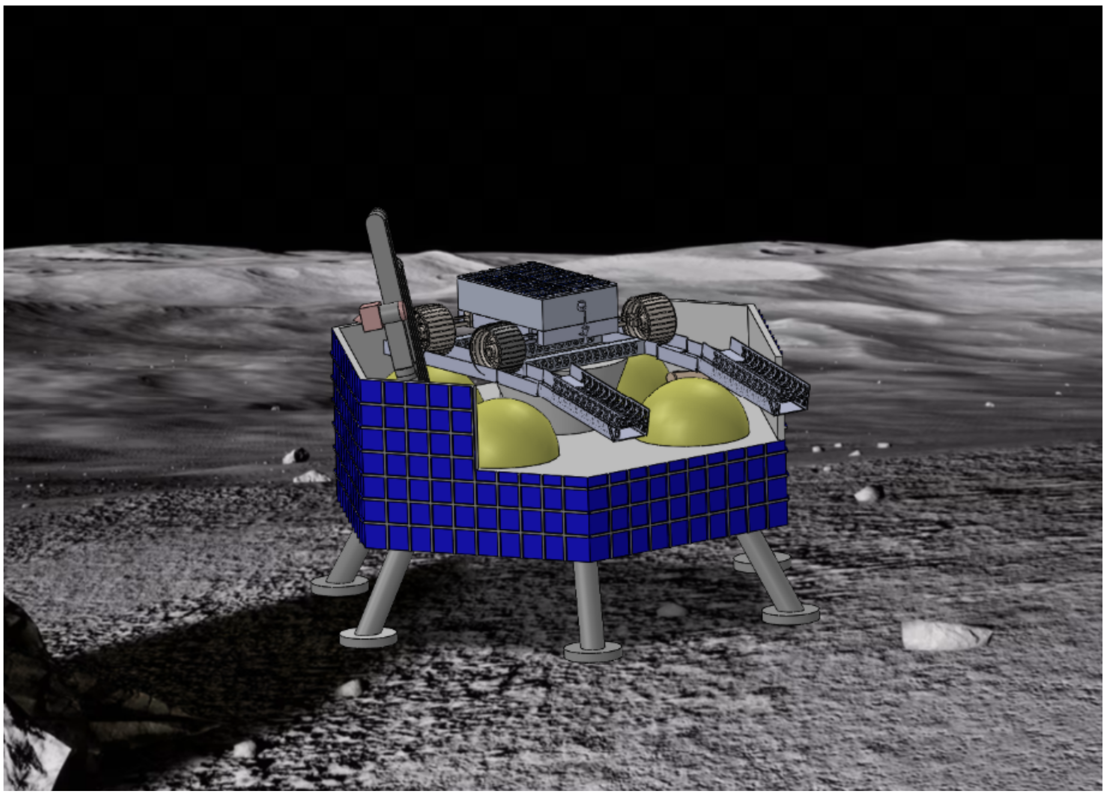

Team Members:

Team Lead: Tyler Requa[1]
tylerrequa1@gmail.com

Anna Ring[1]
Connor Crain[1]
Connor Gibson[1]
Peter Khorani[2]
Virginia Knight[1]
Nguyen Ly[1,2]
James Mitrushi[1]
Riley Vazquez[1]

Faculty Advisor:

Adam Nokes
adamnokes@utexas.edu

[1] Aerospace Engineering (Undergraduate Senior) [2] Physics (Undergraduate Senior)

University of Texas at Austin: DUSTEE

Demonstration of Up-scalable Surface Treatment for Earth–Moon Economy

RASC-AL
Revolutionary Aerospace Systems Concepts Academic Linkage

Objectives & Technical Approach:

- Demonstrate scalable lunar surface hardening via laser and solar sintering technologies
- Generate a comparable dataset across various surface configurations to confirm best method of processing
- Quantify performance with repeatable metrics: compression, LiDAR roughness, and plume response
- Direct comparison of sintering technologies to support future decisions for lunar infrastructure and architecture

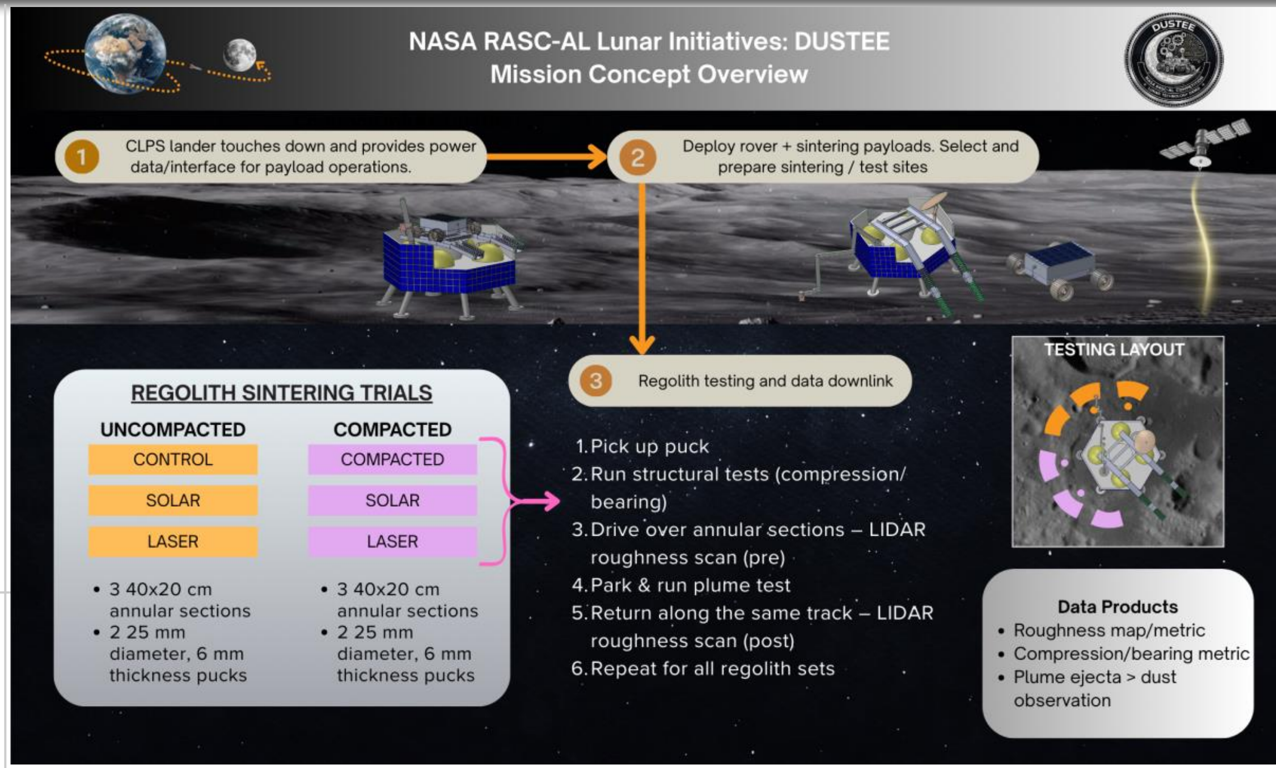

Key Design Details & Innovations:

	Mass (kg)	Power (W)	Cost ($M)
Lander	320	300	148
Rover	400	100	90

- Wheel-based compaction achieves surface densification using existing rover mobility hardware, reducing added mechanisms/mass.
- Common sintering + verification loop: shared deployment architecture for solar/laser, evaluated via LiDAR roughness (pre/post) + compression/bearing + plume/dust observations.
- This single mission produces a direct trade study dataset which can drive future lunar regolith ISRU and infrastructure development

Mission Schedule:

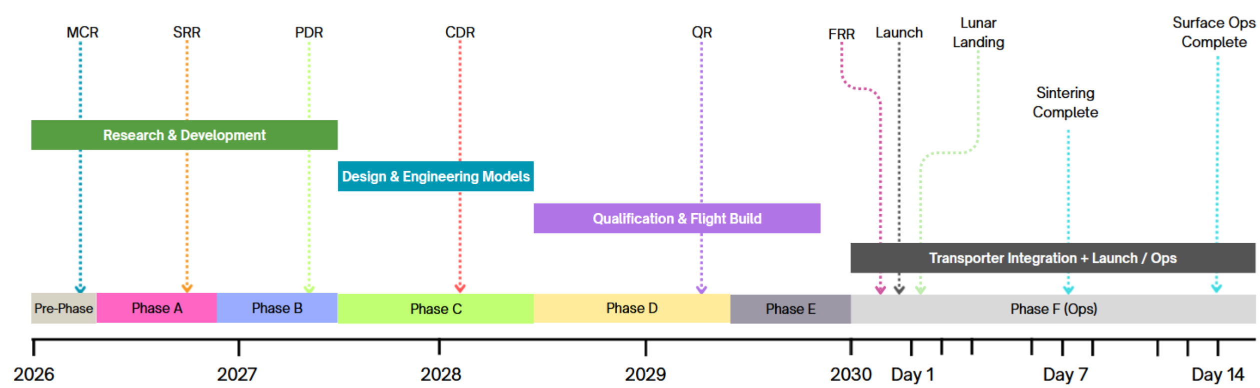

2026 RASC-AL Proposal Compliance Matrix

Lunar Technology Demonstrations Leveraging Common Infrastructure

General Proposal Information	Y/N
Does your submission adhere to the requirements and constraints of the selected topic and the design competition? Does it adhere to the page limitations and formatting guidelines?	Y
Have you proposed synergistic applications of NASA's planned current investments with new innovative approaches / capabilities / technologies to support your proposed solution?	Y
Does your proposal present original engineering analysis of innovative approaches, capabilities and/or new technologies for evolutionary architecture development to enable future missions, reduce cost, and/or improve safety?	Y
Have you provided sufficient justification for your assumptions?	Y
Have you addressed reliability and human safety considerations when trading various design options?	Y
Is your approach guided by sound systems engineering and architectural trades?	Y
Have you documented and justified your technology readiness levels (TRLs) for the technologies associated with your proposed solution?	Y
Are appropriate assessments of costs for technology maturation, system development, and production & operations included in your proposal?	Y
Did you include an appropriate project schedule and test plan with realistic development and annual operating costs (i.e., budget for technology maturation, system development, and production & operations)?	Y
Lunar Technology Demonstrations Leveraging Common Infrastructure Theme	**Page #**
Where does your proposal describe the Lunar Infrastructure Objectives that your concept responds to?	4
Where does your proposal describe the technology demonstration campaign your concept will enable?	4,5, 7-12
Where does your proposal describe the support to both an early lunar ecosystem as well as pathways to industrial-scale operations and/or a robust lunar economy?	12
Where does your proposal describe the infrastructure needs that would be leveraged by your campaign?	12
Where does your proposal describe the common services that would lower mass, cost, and complexity for your campaign?	4

Contents

1 Introduction

1.1 Problem Statement

Earth's moon is a critical stepping stone towards exploring Mars and the wider solar system. It is therefore vital that we master manufacturing techniques and other technologies that will advance us towards a robust lunar economy. On the road to mastering these technologies, however, they must first be tested, analyzed, and iterated upon.

1.2 Lunar Infrastructure (LI) Alignment

An essential prerequisite for erecting complex infrastructure is the ability to manufacture strong and durable surfaces. For example, the construction of roads, landing pads, bricks, walls, and other infrastructure is not possible without first demonstrating this capability. Landing pads, in particular, significantly reduce the plumes generated by spacecraft landings and takeoffs, enabling greater landing precision (LI-5). Roads similarly prevent fine regolith particles from being kicked up and damaging surface hardware, while walls provide barriers that protect humans and sensitive equipment from harmful solar radiation.

To this end, DUSTEE seeks to demonstrate one one of the most promising methods for manufacturing solid surfaces out of lunar regolith: sintering (LI-7). DUSTEE will autonomously manufacture (LI-4) sintered surfaces using both solar and laser sintering, then evaluate their performance relative to each other.

2 Project DUSTEE Concept Overview

2.1 System Architecture Summary

To best accomplish the Moon-to-Mars LI objectives, Project DUSTEE will use the Astrobotic Griffin Commercial Lunar Payload Service (CLPS) lander, complete with a rover storage and deployment system. This common service would greatly reduce the project cost and complexity associated with developing a custom lander; resources can instead be funneled into economical modifications. Figure 1 shows a schematic of DUSTEE's subsystems in action.

Each subsystem houses innovative adaptations of existing, experimentally demonstrated solutions, described in more detail below. Together, these payloads enable a technology demonstration that returns quantitative performance data to determine which method of surface preparation best supports scalable in-situ resource utilization (ISRU) capabilities.

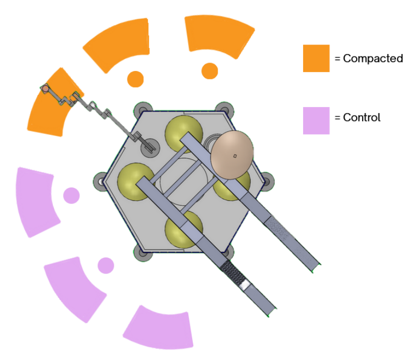

Figure 1: Top-down view of DUSTEE in operation.

2.1.1 Sintering

DUSTEE will sinter regolith into partial annular pads and small pucks around the lander using a hollow titanium arm, directly addressing LI-4 (autonomous construction) and LI-7 (ISRU). In "solar" mode, a deployable parabolic mirror and compound parabolic concentrator (CPC) focus sunlight into a 10 m optical path to the lunar surface. In "laser" mode, a lander-powered continuous-wave (CW) diode laser outputs a ~70 W collimated beam to a ~2 mm spot. The end effector operates ~25-30 cm above the surface, providing an irradiance of $\sim 10^4$ W/m^2 and enabling continuous sintered track formation.

2.1.2 Regolith Preparation

DUSTEE's rover subsystem can produce a compacted surface before sintering begins, providing two data sets to evaluate the effectiveness of the sintering subsystems. Inspired by

Apollo, Perseverance, and VIPER, the rover wheels use a rigid rim-and-hub architecture with low-profile grousers to reduce local stress concentrations and evenly pack loose regolith into a tight region. The separation of drive, steering, and suspension actuation axes allows the rover to exert a controlled rear-wheel force without redistributing the center of mass by lifting the front wheels. Section 4.1 presents the supporting calculations.

2.1.3 Compression Testing

To validate the experimental properties of sintered regolith from simulant studies, DUSTEE's rover carries a compression testing subsystem integrated into the underside of the chassis. A dedicated rover-mounted arm retrieves the puck and brings it into a small testing chamber where structural properties such as Young's modulus, peak compressive strength, failure strain, and qualitative failure modes are measured.

2.1.4 Plume Testing

A primary use case for regolith sintering is landing pads that mitigate plume generation and enhance precision landing capabilities. To evaluate each sintered surface's performance under plume loading, a nozzle on the rear of the rover directs pressurized nitrogen onto each partial annular section. A sensor gate mounted parallel to the ground plane detects the particulate mass ejected during plume interaction.

2.1.5 Roughness Test

Surface roughness is a critical metric for infrastructure such as roads. Roughness is measured using a LiDAR camera mounted on the underside of the rover. The system provides discrete height measurements across the surface, with the standard deviation relative to the mean surface plane yielding a quantitative roughness value.

2.2 Mission Objectives and Success Criteria

DUSTEE's objectives are to (a) identify the most effective surface-preparation method for lunar infrastructure by comparing compaction, solar sintering, and laser sintering, and (b) quantify relevant performance metrics for each configuration using rover measurements of mechanical response, surface roughness, and dust/ejecta response.

The mission is considered successful if it (a) completes the planned configuration strategies (uncompacted vs compacted; none vs solar vs laser), (b) executes the measurement loop for each configuration (compression testing where applicable, pre/post roughness mapping, and plume testing), and (c) returns a comparative dataset that distinguishes the effects of each surface treatment and supports a selection for future infrastructure scalability.

3 Concept of Operations

DUSTEE's surface demonstrations are designed to determine which regolith surface-preparation method is most suitable for scalable lunar infrastructure. Specifically, DUSTEE isolates the effects of ground preparation (uncompacted vs compacted) and processing method (none vs solar sintering vs laser sintering) on the lunar surface, all while holding test geometry and measurement procedures constant across all conditions. These tests produce a quantitative dataset that supports the selection of a method that best improves mechanical integrity, maintains acceptable surface conditions, and minimizes dust response — all key requirements for practical lunar surface infrastructure.

3.1 Surface Operations Timeline

DUSTEE follows a structured development and surface operations timeline spanning research, system maturation, flight qualification, and lunar deployment. The mission progresses through standard NASA design reviews before launch and culminates in a 14-day surface demonstration campaign. Figure 2 displays the timeline.

Phase F0: *Landing Site Selection and Terrain Morphology*. The team will screen south-polar landing zones using Lunar Orbiter Laser Altimeter (LOLA) geodetic topography and illumination modeling to identify a site that maximizes solar availability while meeting landing/traverse hazard limits. The team then characterizes local terrain morphology (slopes, roughness, rock abundance, and shadowing) to select test patches for coordinated lander–rover operations.

Phase F1: *Landing and Initial Checkout*. After CLPS touchdown, the lander completes power, communications, and thermal checkouts, confirming stable operations before any payload deployments occur.

Phase F2: *Rover Deployment and Site Setup*. The rover is deployed near the lander and collects baseline LiDAR documentation of the test surfaces before any sintering occurs. The rover wheels then drive over one side of the test site, compacting half of the testing surface and leaving the other half uncompacted for controllability.

Phase F3: *Lander Arm Sintering Operations*. The lander arm deploys the sintering payload and produces standardized geometries for testing. Sintered pucks are produced for mechanical testing, and partial annular patches are produced for roughness and plume evaluation. Unsintered control surfaces do not require puck retrieval; only the partial annular patches are evaluated.

Phase F4: *Rover Testing Operations*. After sintering operations are complete, the rover performs the tests required to collect the necessary comparative data. This includes retrieving sintered pucks for compression testing, running plume tests, and conducting pre- and post-plume roughness mapping on each patch. This measurement loop is described in Section 3.3.

Phase F5: *Optional Repeats and Post-Night Testing*. The mission concludes with final imagery and telemetry downlink and safe parking of the rover. If the night survival configuration is selected and the rover successfully recovers at sunrise, an optional second measurement loop may be executed on previously tested patches to evaluate whether temperature drops through the lunar night has altered the mechanical or surface properties of sintered regolith. This would provide a secondary dataset on the long term durability of each surface treatment

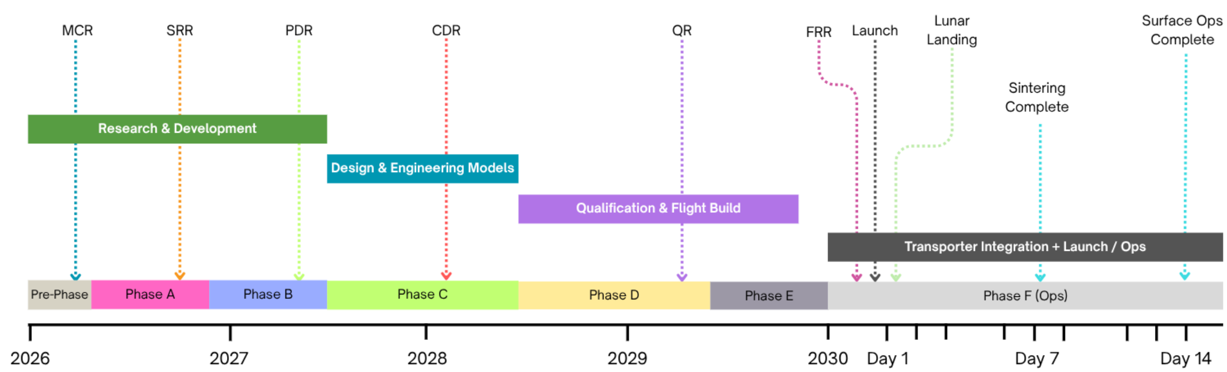

Figure 2: DUSTEE development, launch, and surface operations timeline.

3.2 Regolith Processing Configurations

DUSTEE evaluates six regolith configurations: control (uncompacted), control + solar sintering, control + laser sintering, compacted, compacted + solar sintering, and compacted +

laser sintering.

Each configuration is implemented on the same test site using the Phase F2 split-site approach (uncompacted vs compacted) and Phase F3 processing approach (none vs solar vs laser). For each compaction configuration, DUSTEE produces standardized test articles consisting of two sintered pucks (~25 mm diameter × ~6 mm thickness) for compression testing and three annular surface patches for roughness mapping and plume testing.

3.3 Measurement Loop & Data Products

Expanding on the Phase F4 rover testing operations, the rover executes the following loop: 1) Retrieve a sintered puck from the processed region (if applicable). 2) Perform compression testing on the puck to quantify mechanical response. 3) Traverse the conical patch and measure roughness (pre-plume imaging). 4) Park and run a plume test to measure dust response. 5) Retrace the same path and re-measure roughness (post-plume imaging). 6) Repeat for all regolith configurations.

This produces a consistent dataset for each condition, including measurable outcomes that matter for lunar infrastructure: improved mechanical integrity, reduced surface roughness degradation under disturbances, and reduced dust response. These results support an assessment of surface viability, informing the selection of site-preparation strategies for future lunar infrastructure.

4 Preliminary Design & Demonstration Plan

4.1 Surface Preparation: Wheel-Based Compaction

Figure 3: Rear wheel compaction zone and grouser geometry.

DUSTEE conditions lunar regolith using wheel-based compaction to reduce packing variability prior to sintering [1, 2]. For a 400 kg rover (648 N lunar weight), 60–70% of load is shifted to the rear axle in compaction mode, producing 194–227 N per rear wheel (Appendix A.1.2). With 0.508 m diameter and 0.330 m width wheels (Figure 3), this corresponds to mean contact pressures of 6–14 kPa for effective contact lengths of 0.05–0.10 m (Appendix A.1.4), defining the gravity-limited compaction regime.

The wheel design draws from Apollo and VIPER mobility heritage [3, 4, 5, 6]. Each wheel includes 30 rigid grousers (9 mm wide, 7.6 mm high, 325 mm long) spaced 53 mm apart (Appendix A.1.3), distributing stresses while limiting excavation and promoting near-surface densification. At the particle scale, compaction is achieved through a combination of normal loading and controlled shear deformation. The applied wheel load increases interparticle contact forces, reducing void space and increasing bulk density, while limited slip induces shallow shear displacement that promotes particle rearrangement without significant excavation. The use of discrete grousers concentrates stresses at the contact interface, enhancing near-surface densification while maintaining overall geometric stability of the terrain.

Compaction is performed by the rear wheels at 0.01–0.04 m/s with slip ratios of 0.05–0.12, executing 5–20 parallel passes depending on conditioning level. Shear disturbance is bounded by grouser height (h_g = 7.6 mm; Appendix A.1.5), maintaining modification within millimeter-to-centimeter scale and preventing bulk excavation. Under gravity-limited loading with controlled slip, this approach increases surface stiffness while preserving geometry for sintering.

Rear-axle load biasing is achieved via internal pitch-moment generation rather than center-of-mass translation (Appendix A.1.1). In addition, the compaction force is actively regulated through the rover's suspension architecture. Each rear wheel module integrates drive, steering, and independently actuated suspension elements (Figure 4), enabling modulation of wheel normal force under varying terrain conditions. Drawing from VIPER mobility system principles, integrated torque sensing allows estimation of wheel–ground interaction loads, enabling closed-loop regulation of normal force. This ensures consistent contact pressure across heterogeneous regolith and improves repeatability of the compaction process compared to passive load distribution alone.

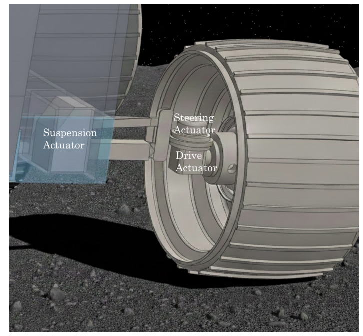

Figure 4: Rear wheel module.

In addition to local wheel–soil interaction, the global compaction strategy is governed by rover geometry and path planning to ensure repeatable and non-interfering surface conditioning. The rover rear wheels are separated by a track width significantly larger than the individual wheel width (0.330 m), resulting in two distinct compaction lanes per pass. This spacing ensures that each rear wheel operates on undisturbed regolith, preventing overlap between adjacent tracks during a single traverse. The lateral gap between the wheels preserves an uncompacted strip, which is subsequently conditioned in later passes.

Compaction is executed using parallel linear traverses across the designated test region. After each pass, the rover laterally offsets by approximately one wheel width, producing adjacent, non-overlapping compaction lanes. This approach ensures uniform coverage while avoiding repeated loading of previously compacted regions, which could otherwise introduce variability in density and surface stiffness.

The extent of lateral disturbance is limited by the grouser geometry and controlled slip conditions. With low-profile grousers and slip ratios maintained between 0.05–0.12, shear deformation remains localized beneath each wheel, with minimal propagation into neighboring regions. As a result, previously compacted tracks remain mechanically independent, preserving the integrity of the conditioned surface.

To ensure experimental repeatability, the rover follows identical paths for compaction and subsequent measurement operations, as described in Section 3.3. This co-registration between compaction tracks and LiDAR roughness scans minimizes spatial variability and allows direct comparison of surface response before and after plume interaction.

This path-planning strategy supports DUSTEE's objective of generating a controlled and comparable dataset across all regolith configurations. By maintaining strict geometric separation between compaction tracks and minimizing disturbance overlap, the system ensures that measured differences in mechanical response, roughness, and plume behavior are driven by the intended surface preparation methods rather than unintended rover-induced effects.

The wheel compaction method (TRL 6) builds directly on flight-proven Apollo and VIPER mobility architectures and has been validated in relevant regolith simulant testing environments.

4.2 Sintering

The main enablers for ISRU in this mission are the sintering devices. The sintering apparatus consists of two separate instruments held on the CLPS: the solar sintering subsystem and the laser sintering subsystem. Both are controlled by a 7DOF robotic arm (RA) held on the top of the CLPS that can rotate up to 225° about its base. The main sintering hardware is

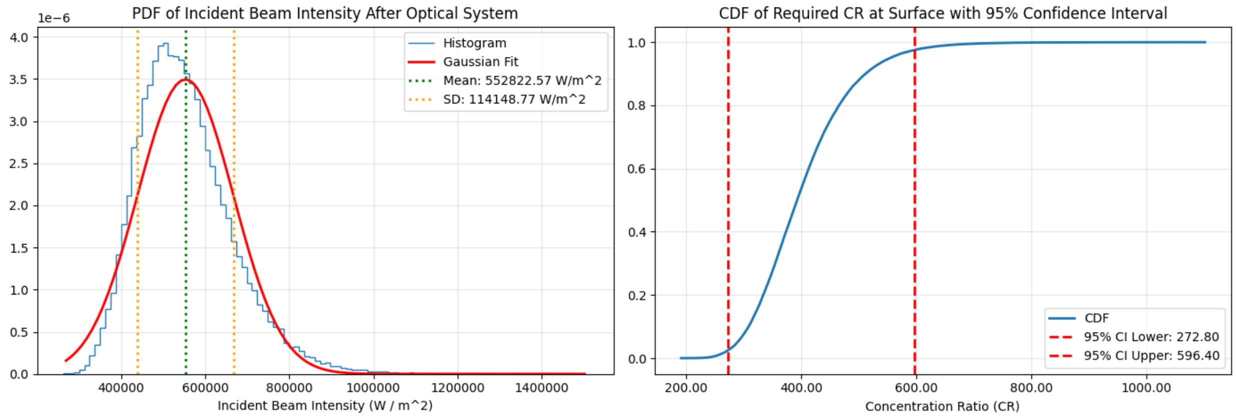

Figure 5: Monte Carlo simulation of surface irradiance.

held at the end of the arm in a sintering compartment, where end effectors are used to swap between the two subsystems.

The robotic arm has a TRL of 7 and is heavily inspired by the Japanese Experiment Module Remote Manipulator System (JEMRMS). The booms are constructed from carbon fiber reinforced plastic (CFRP) tubes, which are stiff, lightweight, and resistant to thermal expansion [source]. The translation speed of the tip can reach a maximum of 60 mm/s; as such, the rastering speed of each sintering method is limited only by the surface heating rate achieved [same].

4.2.1 Solar Sintering

To fulfill Mission Objective [value], DUSTEE carries an optical configuration to harness the energy of the Sun and produce a thin but resilient layer of sintered lunar regolith. The rapid deployment of a surface generator is key to supporting future lunar missions through safer landing zones and dustless travel paths.

Sintering requires a surface temperature of 1323-1473 K based on experiments using mare regolith simulants JSC-1A, OPRL2N, CLRS-1, CLRS-2, DNA, HUST-1, Mare, and EAC-1A, and highlands simulant OPRH2N. However, the requisite irradiance may vary significantly based on the chosen landing site, so a Monte Carlo simulation was performed on 50,000 possible locations (see Appendix A.3) to produce a range of possible beam intensities, shown in Figure 5. A 95% confidence interval of the subsequent CDF yielded a CR of 273.42-597.84 assuming a solar constant of 1370 W/m^2 at the lunar South Pole.

To deliver the necessary concentrated sunlight, DUSTEE combines the flexibility of the robotic arm with a fiber optic cable and a quartz rod end effector. This subsystem has a TRL of 6 based on its successful operation at the Mauna Kea testing site as documented in [7]. All that remains is to deliver the rays to the fiber optic cable whilst satisfying the constraints of the mission enviroment. A trade study (Table 1) was conducted on four primary concentrator types: offset parabolic, Cassegrain, line trough, and Fresnel lens. The nearly horizontal solar elevation angle and lander-restricted ConOps favors the offset parabolic concentrator due to its wide range of focus locations and full surface utilization.

Table 1: Primary Concentrator Trade Study. 4 is the highest possible score.

Optical System	Solar Acceptance	Ease of Deployment	Thermal Efficiency	Dust Tolerance	Technological Maturity	**Total**
Weight	30%	30%	20%	10%	10%	**100%**
Cassegrain	1	2	3	2	3	**2**
Fresnel Lens	3	4	1	1	4	**2.8**
Offset Parabolic	4	3	2	3	2	**3**
Line Trough	2	1	4	4	1	**2.2**

In the final iteration of the solar sintering system, the primary mirror is composed of twelve aluminum "petals" attached to a rotatable core plate, each coated in protected silver to achieve a reflective efficiency of 0.94 without losses due to finite segmentation [7]. The unfolded diameter of the apparatus is 0.9 m, which allows the hinges to fold inward and lock into a segmented, offset parabola with a geometric CR of 515. The mirror is supported by a single arm on a swivel base, giving it a wide range of pointing angles.

The parabolic collector directs incoming sunlight towards the CPC, which acts as a secondary mirror to capture off-axis rays and direct them towards a fiber optic cable attached to its base. The acceptance half-angle of the CPC is a generous ±45° in exchange for a modest CR of 2 [8]. The CPC is made of the same material and coating as the primary mirror, making its reflective efficiency 0.94 as well [7]. It also has an adjustable boom with 2 DOF guided by a light sensor to prevent excessive misalignments.

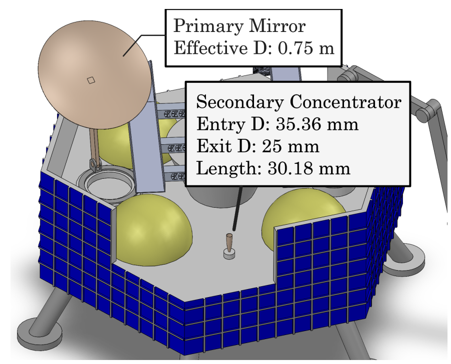

Figure 6: Dimensioned optical components.

Once the concentrated sunlight leaves the CPC, it enters a fiber optic cable that snakes along the exterior of the arm to redirect the beam towards the regolith. The approximately 10 m long cable consists of high OH-content silica fibers (Figure 7) protected by a "buffer" of Tefzel; clamps at the midpoints of each arm section allow it to bend as the robotic arm travels to the designated sintering locations [9]. The efficiency of the fiber is 0.9 when machined to minimize internal reflective losses as well as Fresnel losses at both ends [7].

Inside the sintering compartment, the optic cable is conjoined to a quartz rod that is index-matched to gather the individual outputs of each fiber into one cohesive beam. When the sintering operation begins, an aperture on the bottom of the box slides open before the mirrors align, delivering a near-homogeneous beam to the lunar surface. Assuming minimal pointing errors for the primary mirror, the solar sintering system will deliver about 531 W at the center of the beam and sinter the patch within 17 s. This is close to the optical power of 540 W achieved by the Mauna Kea sintering test [7]. Detailed calculations can be found in the same appendix (A.3).

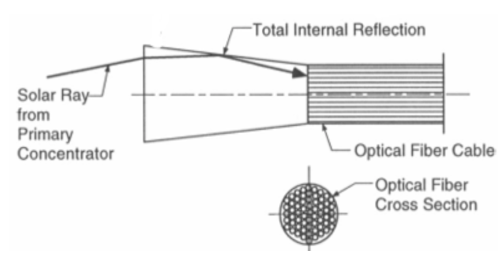

Figure 7: Cross-section of proposed fiber optic cable.

4.2.2 Laser Sintering

The laser sintering subsystem provides illumination-independent processing using a continuous wave (CW) 976 nm stacked InGaAs diode laser [11]. Electrical power is supplied from the CLPS lander DC bus (baseline ~250 W) and conditioned through a dedicated DC–DC stage and current-regulated laser driver within the payload enclosure to produce ~70 W optical output after coupling and transmission losses [11]. Beam conditioning (FAC/SAC collimation, symmetrization, and fiber-coupling) improves pointing stability and coupling efficiency at high power [12, 13]; because these components are mature and widely demonstrated in relevant environments, the laser subsystem is assessed at TRL 5.

At the end effector, the beam is focused to an order-2 mm spot at a nominal 25–30 cm standoff, yielding an irradiance on the order of 2.23×10^3 W/cm^2 for continuous track formation (see Appendix for calculations). Tracks are produced using a serpentine raster: the robotic arm translates at a commanded scan speed (baseline ~10 mm/s) with fixed line spacing/overlap, while laser output is gated or reduced during turnarounds to avoid corner overheating and maintain uniform thermal dose. Power and signal harnessing is routed inside the hollow arm with joint-level spools to manage slack during multi-joint motion; contact surfaces are treated with dry MoS_2 lubricant for low-temperature, heaterless operation [14].

4.3 Verification Instruments

4.3.1 LiDAR Surface Mapping

The roughness measurement subsystem quantifies how each surface patch changes under operational disturbances by generating 3D surface maps before processing, after processing, and after plume exposure.

Using a nadir-pointing LiDAR mounted on the rover's underside (Figure 8), the rover collects overlapping 3D point clouds covering the conical patch footprint. This enables direct comparisons across the six regolith configurations and helps distinguish the effects of compaction and sintering on surface texture and degradation behavior. The same sensor is used to scan each sintered puck's top face prior to compression testing to estimate thickness and tilt, providing a geometry check and reducing uncertainty due to specimen nonuniformity. The LiDAR sensor performs multiple scans and overlaps them to cover the full patch area. Roughness is estimated from small-scale height variations after removing overall slope and curvature, producing a single roughness metric for each patch. The same sensor scans each puck face before compression to estimate tilt and flatness. Specimens outside a defined threshold are flagged as lower confidence.

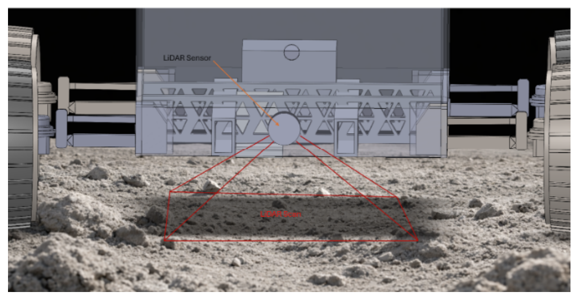

Figure 8: LiDAR sensor mounted on bottom of rover.

4.3.2 Compression Testing

The rover compression test subsystem characterizes the structural properties of sintered regolith pucks produced by the lander. Each specimen is acquired from the surface and placed into a sealed belly-mounted test bay where it is loaded in uniaxial compression. During testing, an in-line load cell records the applied force while an LVDT sensor measures the displacement between the two test plates. The measured force and displacement are converted to engineering stress and strain to estimate modulus, peak strength, and failure behavior [15].

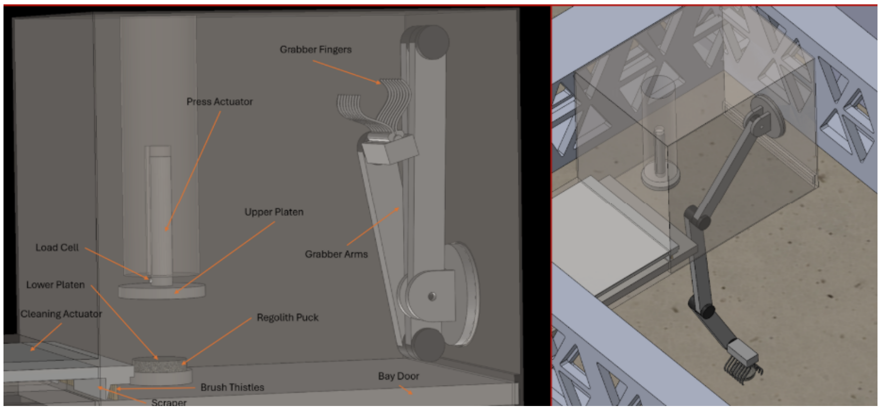

Figure 9: Diagram of compression test subsystem. The left image shows the undeployed state; the right image shows a puck being retrieved.

The rover aligns the bay door over the specimen, and a spring-loaded grabber inspired by Apollo-era sample handling tools [16] retracts the puck into the bay and seats it in a centering nest. The bay closes, and the press applies a seating load, then compresses at a controlled rate while force and displacement are recorded until fracture. After testing, debris is cleared using a Zephyr fiberglass fingerprint brush [17]. The brush can be cleaned in an electrodynamic dust shield dock [19], consistent with modern lunar dust mitigation strategies [18].

4.3.3 Plume Subsystem

The plume subsystem determines the success of different types of sintering in reducing ejecta interaction with landing systems. During testing, a plume nozzle attached to the back end of the rover will release a timed burst of nitrogen gas at the lunar surface. Particles that are kicked up from the surface due to this disturbance are then detected using an ejecta detector on the underside of the rover. This allows for direct comparison of the plumes produced by each sintered surface to those of unsintered regolith, a critical success criterion for decreasing the contamination of lunar hardware [20]. Figure 10 shows the plume nozzle and nitrogen tank integrated into the rover chassis.

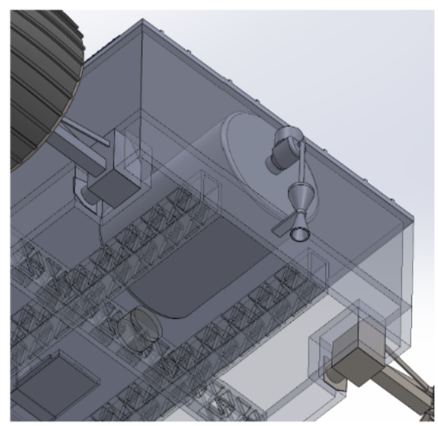

Figure 10: Plume nozzle and nitrogen tank integrated into rover CAD.

The design of the plume nozzle (TRL 6) and the overall test campaign were based on the Physics Focused Ground Test (PFGT) campaign at the Marshall Space Flight Center (MSFC), where a nozzle of similar specifications was used. During this campaign, 10-second bursts of heated nitrogen gas were fired at a lunar simulant in order to approximate the effects of a lunar lander, at mass flow rates of 0.32 and 8 g/s [21]. We chose to design the nozzle around 2-second nitrogen bursts at a higher mass flow rate of 80 g/s for greater predicted regolith disturbances at a lower operating temperature near 292 K. For DUSTEE's test campaign, a minimum of one 2-second plume test will be conducted for each of the six annular sections of regolith.

Nozzle sizing was done using basic converging-diverging nozzle equations with the properties of nitrogen at 300 K used as inputs [22, 23]. Other relevant inputs, such as the nozzle exit height to nozzle exit diameter and the exit area to throat area ratios, were taken directly from the PFGT testing campaign [21]. The exact calculations used for nozzle sizing can be found in Appendix 6.2.1. The result was a nozzle with a 16.2 cm length inlet-to-exit, a 0.75 cm throat diameter, and a 4.20 cm exit diameter, capable of providing 2-second bursts of nitrogen at 6.45 m/s exit velocity and 5.12×10^{-2} N force. It is important to note that these calculations for expected performance are based on ideal rocket nozzle equations for a nozzle on the lunar surface.

We then sized the plume system's nitrogen tank according to the nozzle sizing. Given the minimum of six plume tests for two seconds each at a nozzle mass flow rate of 80 g/s, 0.96 kg of nitrogen will be consumed during testing. However, in order to ensure nitrogen bursts of equal strength, a pressure regulator and solenoid valve will be required inline between the tank and nozzle, as well as additional nitrogen mass to maintain tank pressure during testing. Accounting for this excess nitrogen plus margin, the total mass of N_2 will be 1.2432 kg at beginning of life. When taking into account this nitrogen mass, the desired nozzle inlet pressure of 60 PSI, and assuming an average surface temperature of 270 K near the lunar south pole, the tank in the plume system's preliminary design will have a 17.78 cm diameter, 48.26 cm length, and an internal volume of 7362.38 cubic cm [24, 25]. Detailed tank sizing calculations can be found in Appendix A.2.1.

Figure 11: Still image of nozzle testing

To verify our design work, we 3D-printed our nozzle and tested it with lunar simulant to ensure that the nozzle sizing and inlet velocity were correct. For lunar surface operations, the main concern is the reaction of the sintered surface to either direct impingement of a plume several nozzle lengths away or to continued impingement on a closer surface [29]. For our testing, the goal was to determine the amount of ejecta liberated from the surface within 2 seconds of impingement on a surface several nozzle lengths away. When tested in the Earth's atmosphere, the selected plume nozzle operated best at approximately 60 PSI and 3 inches above the simulant surface, which is a higher pressure and smaller distance from the lunar surface, therefore requiring a larger mass flow rate (80 g/s) than in our initial calculations suggested. However, the force imparted on the lunar surface by the nozzle will be much larger on the moon than on Earth due to the much higher ambient pressure on Earth [23]. Taking into account the expansion that will occur past the end of the nozzle on the lunar surface, the increased distance above the ground (when compared to our test campaign), along with the calculations in A.2.1, we are confident that the nozzle will perform adequately on the lunar surface running at a nozzle inlet pressure 60 PSI. In other words, our Earth-based testing validates our nozzle design at an inlet pressure of 60 psi because we expect the force imparted on the ground to be much larger in the lunar environment, even accounting for the increased ground-nozzle separation. Figure 11 shows a still image captured during experimental validation.

The final component of the plume subsystem is the ejecta detector mounted on the underside of the rover at the end opposite the plume nozzle. The ejecta detector was modeled on the Grain Impact Analyser and Dust Accumulator (GIADA) instrument from the Rosetta mission, which was designed to detect dust grains in the tail of a comet (TRL 7 for our purposes, not 9, since it has not been demonstrated in the lunar environment) [26]. The detector's architecture consists of an optical gate and a detector plate, mounted with the instrument's aperture (20 cm x 30 cm) facing the ground beneath the rover, as shown in Figure 12.

The optical gate consists of four lasers paired with collimators mounted along the aperture's long side to generate a continuous light curtain. On the short sides of the aperture, parallel with the lasers, are four photodiode detectors (eight total), which will detect light scattered by incoming dust grains.

Once grains pass through this optical gate, they will collide with the aluminum detector plate, mounted atop five piezoelectric sensors. This architecture allows us to determine dust particle count (via the optical gate), dust particle velocity distribution (gate-plate separation divided by time between gate-plate detection), and dust particle mass distribution (impulse divided by velocity for each grain detection) for each annular section of processed regolith.

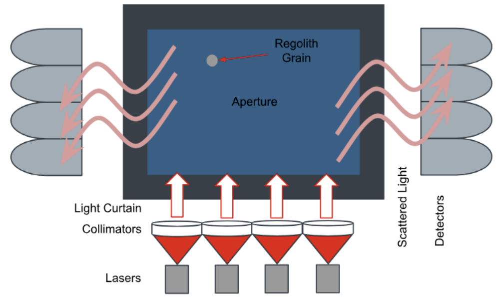

Figure 12: Diagram of the ejecta detector's optical gate

4.4 Lunar Night Survival

A key design goal for DUSTEE is the ability to survive the lunar night, enabling post night data recovery and extended surface operations if nominal daytime activities are completed ahead of schedule. The survival architecture is designed around reducing the design driving eclipse duration through deliberate site selection, and minimizing night time power load by only powering what is necessary for vehicle survival.

4.4.1 Eclipse Duration Reduction via Site Selection

Full lunar night at the equator spans approximately 354 hours, which would require an impractically large battery to survive. The optimal landing site for a mission capable of surviving the night is therefore a high illumination ridge at the lunar south pole, where local topography limits eclipse durations to on the order of 72 to 120 hours [25]. This is the same strategy employed by VIPER, which was designed to park at pre identified high altitude south polar sites where darkness lasts only three to four Earth days rather than the full 14 day lunar night [28]. DUSTEE's survival system is sized to this south polar worst case eclipse period as the baseline design point.

It should be noted that night survival is an optional mission extension rather than a driving requirement. DUSTEE's primary science objectives can be fully accomplished at mid-latitude landing sites within a single lunar day, without any night survival hardware. The south pole is the preferred site for maximizing solar availability and therefore night survival feasibility, but the mission architecture does not preclude a mid-latitude deployment if programmatic or landing constraints favor it.

4.4.2 Battery Sizing and Chemistry

DUSTEE uses lithium-ion (Li-ion) cells for night survival energy storage, consistent with heritage on VIPER, Curiosity, and Perseverance [28, 14]. Li-ion offers high energy density ($\sim$200 Wh/kg) and is rechargeable from the solar array upon sunrise. A critical constraint is that Li-ion cells must remain above $\sim -20^\circ$C during discharge and above $\sim 0^\circ$C during recharge to prevent permanent capacity degradation; accordingly, the battery pack includes a dedicated resistance heater, which constitutes the single largest survival load. The battery is co-mounted inside the rover electronics enclosure so that passive waste heat from avionics during standby reduces the heater duty cycle. Full sizing calculations are provided in Appendix A.4; for a representative 96-hour worst-case south polar eclipse at 25% margin, the required storage is $\approx$2.5 kWh, yielding a battery mass of approximately 15.75 kg.

This configuration supports a surface mission of up to approximately 100 days, comparable to VIPER's planned operational lifetime [4, 28], assuming nominal daytime recharging between eclipse periods.

Table 2: DUSTEE survival mode power budget (eclipse operations only).

Platform	Load	Power (W)
Rover	Battery pack heater	10
Rover	Electronics enclosure heater	8
Rover	Wake-up avionics (minimal)	3
Rover	**Rover survival total**	**21**

All non-essential systems — sintering payloads, verification instruments, mobility drives, and plume hardware — are fully powered down at eclipse entry. The rover executes a pre-eclipse parking maneuver to the highest-illumination position reachable within its traverse range.

4.4.3 Passive Thermal Control

The rover chassis is blanketed in multi-layer insulation (MLI) to reduce radiative loss to the lunar surface, which reaches ~90 K during night at the south pole [25]. Electronics enclosure interfaces facing the regolith are further isolated using aerogel panels, which provide high thermal resistance at low mass penalty. Together, the passive insulation stack reduces the required heater power shown in Table 2, improving battery margin.

4.4.4 Lander Night Operations

The Astrobotic Griffin CLPS lander is not designed for full night survival and enters full dormancy at eclipse entry. Rather than relying on the lander to relay communications, the rover maintains a direct-to-Earth (DTE) link throughout the night using an onboard X-band high-gain antenna. This matches the VIPER mission architecture, which also used an X-band DTE system rather than a lander relay [28]. The south pole geometry makes this particularly viable. Due to lunar libration, Earth remains nearly fixed near the horizon as seen from a south polar site, providing essentially continuous Earth visibility rather than the intermittent contact windows that would be present during equatorial missions. During night, only health and status telemetry are downlinked, keeping antenna power demands low. Should the lander also survive to sunrise, the rover can re-interface with lander power and resume normal operations. Lander survival is treated as a mission bonus rather than a requirement, and it is not expected of the Griffin lander.

4.4.5 Autonomous Sunrise Recovery

After the eclipse, wake-up is triggered autonomously by a photovoltaic sense circuit on the rover solar array. When the open circuit voltage exceeds a preset illumination threshold, the avionics board powers on, runs a system health check, and initiates the battery recharge sequence. This means no ground command is required to exit survival mode. Full operational readiness is restored once the battery state of charge exceeds 80%, at which point the rover resumes the Phase F4 measurement loop from the last completed checkpoint stored in non-volatile memory.

4.5 Cost Assessment and Margin Assumptions

Costs are estimated using an analog-based work breakdown structure, with the CLPS lander services anchored to heritage pricing for Astrobotic's Griffin lander and the rover development/integration cost scaled from publicly reported VIPER rover R&D costs [5, 2]. DUSTEE also reports unique lander/rover payload development and integration costs, environmental test and field-validation costs, and surface-operations costs, with an explicit 30% cost margin consistent with current maturity. The mass column (*Wt.*) in Table 1 is expressed as a percentage of the 1000 kg CLPS payload limit to demonstrate that the flight system remains below 90% allocation, preserving headroom for growth and additional components.

Table 3: DUSTEE Mission Cost summary. A cost margin of 30% is included in this table.

Budget Element	Cost ($M)	Power (W)	Wt.	Basis
CLPS lander services + delivery	110	300 (avail.)	24%	Delivery + lander services.
Lander processing payloads	38	≤290 (peak)	8%	Arm + sintering
Rover platform (mobility + avionics)	60	100 (avail.)	30%	Chassis, mobility, power, comms.
Rover verification payloads	30	≤60 (peak)	10%	LiDAR + compression + plume + puck handling.
Environmental test campaign	20	–	–	TVAC + dust + field demo.
Surface operations	10	–	–	Surface ops execution

4.6 Risk Assessment and Mitigation

Figure 13 shows the comprehensive risk assessment and mitigation plan for DUSTEE. Threats to the mission objectives were categorized by subsystem and depicted on a risk matrix before and after countermeasures. The full table accompanying this chart can be found in Appendix A.5.

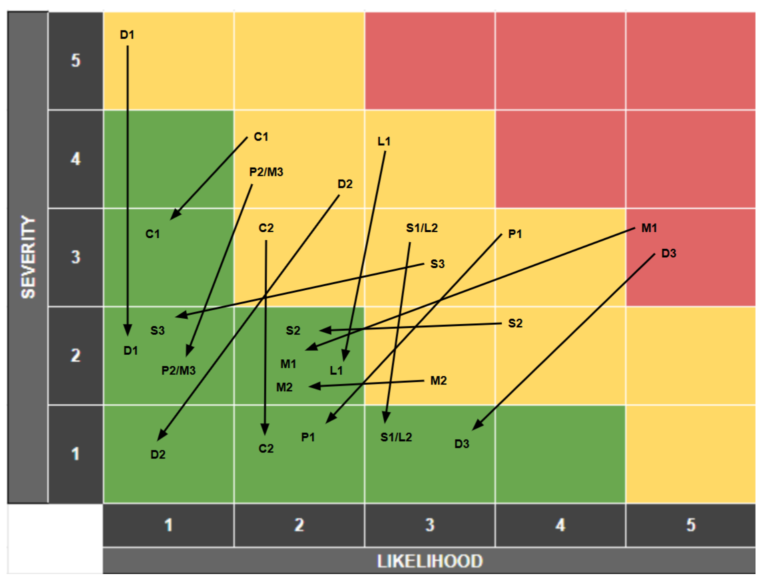

Figure 13: Risk matrix for DUSTEE operations.

The most critical issues are related to dust contamination, whether it be the compression testing chamber (M1), the initial CLPS landing (D3), or the plume detector (P1). Dust tolerance is a key aspect of the DUSTEE mission, so multiple preventative strategies exist for each subsystem. In particular:

The chamber uses a Zephyr fiberglass fingerprint brush to clear the testing area, which is then cleaned in an electrodynamic dust shield dock [17][18][19].

The primary mirror (unfolded) and the CPC are each housed in separate containers to prevent contamination, while the end effectors are covered by a mechanical aperture until the start of sintering.

The plume detector has a short baffle around the detector area to constrain the travel path of the lunar dust, ensuring that electronic contamination remains at a minimum [26].

Other subsystem safety devices, such as the plume nozzle pressure regulator (risk P2) and the sintering compartment heat pipes (risks S3 and L1), ensure that the science mission can proceed as planned with minimal disruption to neighboring instruments and the CLPS lander.

5 Conclusion and Path Forward

5.1 Mission Conclusions

The DUSTEE mission serves as a preliminary testbed for scalable lunar construction, evaluating both solar and laser sintering in conjunction with controlled ground preparation methods to determine the most effective pathway for large-scale infrastructure development. By directly comparing compacted and non-compacted regolith processing across multiple annular test sections, the mission establishes quantitative performance metrics for surface stabilization, structural strength, and plume mitigation.

These findings address a foundational gap in lunar surface architecture. Early infrastructure depends on stable, repeatable, and dust-resistant surfaces built from in-situ regolith, yet the tradeoff between energy source and preparation method remains largely unvalidated in a relevant environment. By experimentally distinguishing how each treatment affects structural integrity and operational surface performance, DUSTEE directly informs the design of landing pads, roadways, habitat foundations, and other surface systems required for long-duration lunar operations.

5.2 Future Work and Scalability

Once the best-performing treatment is identified, the next step is to move from comparative testing to a production-oriented system. The scaled architecture has three elements: (1) a preparation rover for clearing, grading, and compaction, (2) a sintering platform built around the chosen energy source with parallel processing arms, and (3) a validation subsystem that checks flatness, strength, and ejecta deterrence in real time. Together, they form an autonomous construction platform that handles preparation, fabrication, and verification as it moves across the site. The architecture is modular and linearly scalable by adding sintering arms: a single unit suffices for a landing pad or short roadway, while a coordinated fleet can handle transportation corridors, launch zones, and protective barriers.

The value of that scalability also shows in the economics. Launching mass to the lunar surface costs on the order of a million dollars per kilogram, so infrastructure built from local regolith rather than shipped from Earth is a major cost reduction, especially for large, heavy structures like landing pads, roads, and shielded habitats.

The value goes beyond cost. A sintered landing pad shields nearby hardware from the descent plume. A sintered roadway keeps rover wheels from kicking up dust that wears down exposed equipment. Layered sintered material shields habitats from radiation without additional launched mass. Each of these addresses a failure mode already observed in prior lunar missions, and each becomes more critical the longer a mission remains on the surface. By validating the methods behind these structures, DUSTEE lays the groundwork for the infrastructure that a sustained lunar presence will ultimately depend on.

A Appendix A - Calculations

A.1 Wheel-Based Compaction Calculations

This section provides the governing relations and numerical bounds used for the wheel-based compaction subsystem. Relations assume quasi-static operation under lunar gravity.

A.1.1 Load redistribution with internal pitch moment

To quantify rear axle load biasing during compaction mode, the rover is modeled as a rigid body supported by front and rear axle normal forces.

Total lunar weight is:

$$W = mg_L, \quad g_L = 1.62 \text{ m/s}^2 \tag{1}$$

For $m = 400$ kg:

$$W = 400 \times 1.62 = 648 \text{ N} \tag{2}$$

Vertical force equilibrium:

$$N_f + N_r = W \tag{3}$$

Taking moments about the rear axle:

$$N_f L = W x_{CG} - M_A \tag{4}$$

Solving:

$$N_f = \frac{W x_{CG} - M_A}{L} \tag{5}$$

$$N_r = W\left(1 - \frac{x_{CG}}{L}\right) + \frac{M_A}{L} \tag{6}$$

Continuous front-wheel contact requires:

$$N_f \geq 0 \tag{7}$$

These relations show that the rear axle normal load increases linearly with the applied internal pitch moment, while the total vehicle weight remains fixed.

A.1.2 Rear wheel normal-load bounds in compaction mode

During compaction mode, a rear axle load fraction β is commanded:

$$\beta \in [0.60,\ 0.70] \tag{8}$$

Per-wheel rear normal load:

$$N_w = \frac{\beta W}{2} \tag{9}$$

Evaluating bounds:

$$N_{w,\min} = \frac{0.60 \times 648}{2} = 194.4 \text{ N} \tag{10}$$

$$N_{w,\max} = \frac{0.70 \times 648}{2} = 226.8 \text{ N} \tag{11}$$

These values bound the achievable compaction load under quasi-static operation.

A.1.3 Grouser spacing

For wheel diameter $D = 0.508$ m and grouser count $N_g = 30$:

$$s_{\text{circ}} = \frac{\pi D}{N_g} = \frac{\pi \times 0.508}{30} = 0.0532 \text{ m} \tag{12}$$

$$\Delta\theta = \frac{2\pi}{N_g} = 0.2094 \text{ rad} \tag{13}$$

The resulting 53 mm circumferential spacing produces regularized contact intervals during rotation.

A.1.4 Mean contact pressure bounds

Mean rear-wheel contact pressure is approximated as:

$$p = \frac{N_w}{b\,\ell_c} \tag{14}$$

Where:

$$b = 0.330 \text{ m}, \quad \ell_c \in [0.05,\ 0.10] \text{ m}$$

Contact area bounds:

$$A_{\text{min}} = 0.330 \times 0.05 = 0.0165 \text{ m}^2 \tag{15}$$

$$A_{\text{max}} = 0.330 \times 0.10 = 0.0330 \text{ m}^2 \tag{16}$$

Pressure extrema:

$$p_{\text{min}} = \frac{194.4}{0.0330} = 5.9 \text{ kPa} \tag{17}$$

$$p_{\text{max}} = \frac{226.8}{0.0165} = 13.8 \text{ kPa} \tag{18}$$

These bounds demonstrate that compaction stresses remain within a gravity-limited distributed near-surface regime.

A.1.5 Geometric disturbance bound

Shear-driven disturbance depth during compaction is bounded by grouser height:

$$z_{\text{shear}} \le C_h\, h_g \tag{19}$$

Where:

$$h_g = 7.6 \text{ mm}$$

Substituting:

$$z_{\text{shear}} \le C_h(7.6 \text{ mm}) \tag{20}$$

For $C_h \sim 1$–2, disturbance depth remains on the order of millimeters, supporting the operational constraint that rut depth should not exceed nominal grouser height.

A.2 Plume System Calculations

This section provides the equations used to determine the required sizing for all elements of the plume subsystem.

A.2.1 Nozzle Sizing

The following values were taken from NASA's PFGT experiments for the largest surface disturbance during testing.

$\frac{h_e}{d_e}$	$\frac{A_e}{A_t}$	γ	R (J/kgK)
8.0	31.7	1.4	296.8

Table 4: Values from PFGT experiments and nitrogen specific properties [21, 23]

Where h_e is the nozzle exit height from the lunar surface, d_e is the exit diameter, A_e is the exit area, A_t is the throat area, γ is the ratio of specific heats, and R is the gas constant for nitrogen.

The following assumptions were made: nitrogen behaves as an ideal gas undergoing steady, quasi-one-dimensional, adiabatic flow with constant specific heats through a non-ablating nozzle [23].

The total-to-static temperature relation is

$$T_0 = T_x \left[1 + \frac{1}{2}(\gamma - 1)M_x^2\right] \tag{21}$$

With

$$M_x = 1, \quad T_0 = 300 \text{ K}, \quad \gamma = 1.4 \tag{22}$$

This yields

$$T_x = 360 \text{ K} \tag{23}$$

The total-to-static pressure relation is

$$p_0 = p_x \left[1 + \frac{1}{2}(\gamma - 1)M_x^2\right]^{\gamma/(\gamma-1)} \tag{24}$$

With

$$M_x = 1, \quad p_0 = 20 \text{ psi}, \quad \gamma = 1.4 \tag{25}$$

This gives

$$p_x = 10.57 \text{ psi} \tag{26}$$

The speed of sound is

$$a = \sqrt{\gamma R T} \tag{27}$$

Thus at the throat,

$$v_t = a_t = \sqrt{\gamma R T_t} \tag{28}$$

With

$$\gamma = 1.4, \quad R = 296.8 \text{ J/kgK}, \quad T_t = 360 \text{ K} \tag{29}$$

This gives

$$a_t = 1.83 \text{ m/s} \tag{30}$$

The area–Mach relation is

$$\frac{A_e}{A_t} = \frac{1}{M_e}\left[\frac{1+\frac{1}{2}(\gamma-1)M_e^2}{(\gamma+1)/2}\right]^{\frac{\gamma+1}{2(\gamma-1)}} \tag{31}$$

Using $\frac{A_e}{A_t} = 31.7$, the exit Mach number was solved as

$$M_e = 1.83 \times 10^{-2} \tag{32}$$

The exit diameter was selected as

$$d_e = 42 \text{ mm} \tag{33}$$

Thus

$$A_e = \frac{\pi d_e^2}{4} = 1385.44 \text{ mm}^2 \tag{34}$$

and

$$A_t = 43.70 \text{ mm}^2, \quad d_t = 7.46 \text{ mm} \tag{35}$$

The exit velocity was determined using the mass flow relation

$$F = \dot{m} v_e \tag{36}$$

With $\dot{m} = 8$ g/s, the final exit velocity is

$$v_e = 6.45 \text{ m/s} \tag{37}$$

Therefore, the plume force on the lunar surface is

$$F = 5.16 \times 10^{-2} \text{ N} \tag{38}$$

These calculations are the ideal nozzle sizing calculations so actual performance on the lunar surface is different [30]. However, to find the approximate efficiency of the nozzle after the throat we use

$$\lambda = 0.5(1 + \cos(\alpha)) \tag{39}$$

Where λ is the efficiency of the nozzle after frictional losses and α is the nozzle's conical half-angle. By aiming for a half angle of about 15 degrees (0.262 rad), we find

$$\lambda = 0.983 \tag{40}$$

From here the length of the nozzle is

$$L = \frac{\frac{d_t}{2}(\sqrt{\frac{A_e}{A_t}} - 1) + \frac{d_e}{2}\sec(\alpha - 1)}{\tan(\alpha)} \tag{41}$$

Which gives

$$L = 138.05mm \tag{42}$$

A.2.2 Nitrogen Tank Sizing

At minimum six 2-second plume tests will be conducted at a mass flow rate of 80 g/s.

$$m_{\text{test}} = 6 \times 2\text{ s} \times 80\text{ g/s} = 0.96\text{ kg} \tag{43}$$

To maintain regulated pressure during testing, the end-of-life (EOL) tank pressure must be at least twice the regulated pressure [24]. For a regulated pressure of 60 psi, the minimum EOL pressure is 120 psi.

Using the ideal gas law,

$$PV = nRT \tag{44}$$

With

$$P = 827371\text{ Pa}, \quad V = 0.00736\text{ m}^3, \quad T = 270\text{ K} \tag{45}$$

Solving gives

$$n = 2.7127\text{ mol} \tag{46}$$

The corresponding EOL nitrogen mass is

$$m_{\text{EOL}} = 0.0760\text{ kg} \tag{47}$$

Adding testing mass and 20% margin,

$$m_{\text{BOL}} = (0.96 + 0.0760) \times 1.2 = 1.2432\text{ kg} \tag{48}$$

Then, again using the ideal gas law, the beginning-of-life (BOL) pressure using this BOL mass is

$$P_{\text{BOL}} = 13.54 \times 10^6\text{ Pa} = 1963\text{ psi} \tag{49}$$

Since an Airgas size 40 cylinder is rated to 2015 psi, this configuration provides sufficient pressure margin. The selected tank dimensions are 17.78 cm diameter, 48.26 cm length, and 7362.38 cm^3 internal volume [24].

A.3 Sintering Calculations

A.3.1 Solar Sintering Calculations

This section assumes the following:

1. The solar intensity is constant during the sintering period.
2. The subsystem is required to sinter a puck within $t = 60$ s.
3. The puck is uniformly heated by the sintering apparatus. Although the beam profile is not cylindrical (see Section 4.2.1), the RA can adjust the height of the rod end until it is nearly uniform.
4. The regolith is approximated as a thermally thick body for conductive heat transfer. The depth (d) of the sintering layer (6 mm) is negligible compared to the depth of the lunar

topsoil.

5. The initial temperature (T_0) is 387 K.

6. The solar constant (I_0) is 1370 W/m^2.

The energy balance (Eq. 50) for sintering is:

$$\alpha I = \Phi_E + \Phi_R + \Phi_C \tag{50}$$

where I is the desired solar intensity at the surface, Φ_E is the time-averaged input flux

$$\Phi_E = \frac{\rho d c_p (T - T_0)}{t} \tag{51}$$

Φ_R is a conservative estimate of the radiative heat flux

$$\Phi_R \approx \sigma \varepsilon T^4 \tag{52}$$

and Φ_C is a time-averaged conservative estimate of the conductive heat flux

$$\Phi_C \approx \frac{k(T - T_0)}{\sqrt{\pi \alpha_t t}} \tag{53}$$

Here, α_t is the thermal absorptivity, defined as:

$$\alpha_t = \frac{k}{\rho c_p} \tag{54}$$

To capture the variability of lunar conditions, a Monte Carlo simulation with 50,000 data points was performed using the following distributions:

1. The final temperature (T) is uniformly distributed from 1373 – 1423 K.

2. The properties below obey a Gaussian distribution:

   (a) Mean density (ρ) of 1500 kg/m^3, standard deviation of 50 kg/m^3.
   (b) Mean specific heat capacity (c_p) of 800 J/(kg K), standard deviation of 125 J/(kg K).
   (c) Mean emissivity (ε) of 0.85, standard deviation of 0.035.
   (d) Mean absorptivity (α) of 0.57, standard deviation of 0.09.
   (e) Mean thermal conductivity (k) of 0.0074 W/(m K), standard deviation of 0.00074 W/(m K).

Using the values defined above, the mean solar intensity at the surface is ~ 553 kW/m^2 after losses are accounted for, in accordance with the PDF copied here for convenience. The actual distribution is skewed towards the lower end, with a Gaussian fit producing a standard deviation of ~ 114 kW/m^2. Integrating the PDF over the entire domain yields a 95% confidence interval of approximately [374, 817] kW/m^2.

Define the concentration ratio (CR) as:

$$CR = \frac{I}{I_0} = \frac{A}{A_0} = \csc^2(\theta) \tag{55}$$

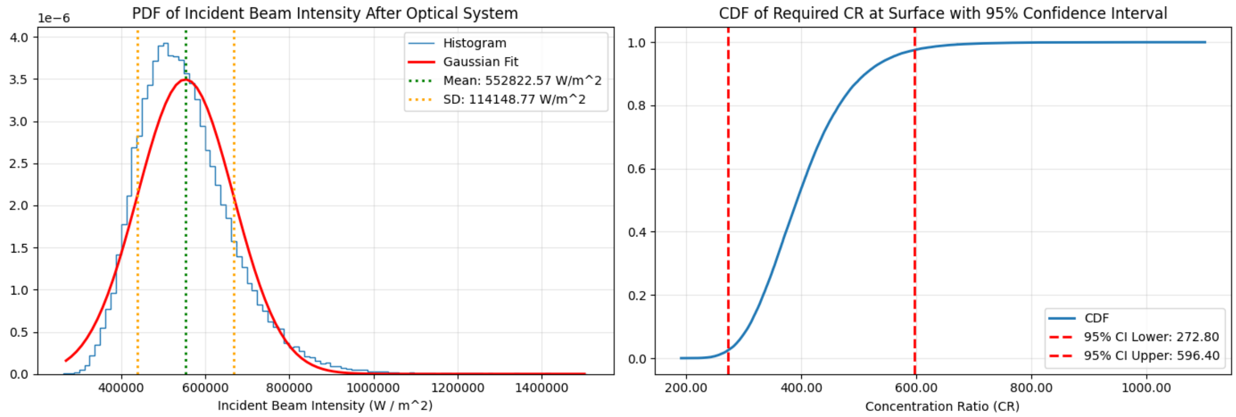

Figure 14: Monte Carlo simulation of surface irradiance.

The left fraction is the standard definition using relative intensities. The right fraction is the geometric definition for sizing the primary mirror, while the rightmost term is the theoretical relation for an axisymmetric, circular CPC given its acceptance half-angle θ.

From the standard definition, the required total concentration ratio ranges from 272.8 to 596.4, which means the primary mirror must provide at least a 136.4× to 298.2× boost in intensity. This report errs on the side of caution and adapts a conservative 300× CR design criteria for the offset parabola. Tying this to the geometric definition forces the mirror to have an effective surface area (magnitude of area vector) of $\sim 0.2945 \text{ m}^2$, making the diameter of a circular extrusion into a full paraboloid at least 0.612 m.

The current design adds an additional "safety factor" of 1.5 to the effective surface area, allowing for the circular cut to be 0.75 m in diameter. However, the feasibility of deploying a perfectly smooth offset parabolic mirror is significantly weaker compared to unfolding segments and interlocking them in place. The James Webb Telescope's primary mirror is a prime example of a successful segmented design and is the driving motivation behind the primary concentrator in Figure 6.

The petals of the primary mirror form the shape of a regular octagon with a projected side length (s) of 0.324 m. This results in an effective area of $\sim 0.506 \text{ m}^2$ using the formula below:

$$A = 2(1 + \sqrt{2})s^2 \tag{56}$$

As such, the geometric CR is ∼ 515 before the CPC, making the total CR 1030.

In an ideal environment with *perfect* solar tracking, the only attenuation would come from the silver coating ($\eta_{\text{Ag}} = 0.94$), the segmentation of the mirror ($\eta_{\text{seg}} \approx 0.925$), Fresnel and internal reflection losses in the cable ($\eta_{\text{fiber}} = 0.9$), and the cable-quartz interface ($\eta_{\text{int}} = 0.98$). Using the solar constant of 1370 W/m^2 from before, this yields a power of 531 W at the quartz rod end, similar to that produced in [6].

To determine the exposure duration for sintering, we assume that the regolith properties are at their mean values in the Monte Carlo simulation and the final surface temperature is 1373 K. Eq. 50 is a nonlinear equation in terms of t, so a Newton-Raphson root finding method on $f(t) = \alpha I - \frac{531 \text{ W}}{490.8 \text{ mm}^2}$ reveals that the surface will reach the sintering threshold after ~ 16.66 s, well within the 60 s requirement.

A.3.2 Laser Sintering Calculations

This subsection provides the governing relations used to size the CW laser sintering operating point reported in Section 4.2.2. The calculations below use the baseline design values:

$$P_{\text{bus}} \approx 250\ \text{W}, \quad P_{\text{opt}} \approx 70\ \text{W}, \quad d \approx 2\ \text{mm}, \quad v \approx 10\ \text{mm/s}$$

where P_{bus} is the electrical load drawn from the lander payload bus, P_{opt} is the delivered optical power at the end effector, d is the surface spot diameter, and v is the commanded raster speed.

Electrical-to-optical efficiency. The end-to-end efficiency (including wall-plug efficiency and optical coupling/transmission losses) is:

$$\eta_{\text{tot}} = \frac{P_{\text{opt}}}{P_{\text{bus}}} \tag{57}$$

Evaluating:

$$\eta_{\text{tot}} = \frac{70}{250} \approx 0.28 \tag{58}$$

This net efficiency is consistent with a high-power diode source (wall-plug efficiency) combined with additional coupling/transmission losses in beam-conditioning optics and the delivery path.

Surface irradiance. Assuming a circular spot with diameter d, the illuminated area is

$$A = \pi \left(\frac{d}{2}\right)^2 \tag{59}$$

For $d = 2\ \text{mm} = 2 \times 10^{-3}\ \text{m}$:

$$A = \pi(1 \times 10^{-3})^2 = 3.14 \times 10^{-6}\ \text{m}^2 \tag{60}$$

The irradiance at the surface is

$$I = \frac{P_{\text{opt}}}{A} \tag{61}$$

Thus:

$$I = \frac{70}{3.14 \times 10^{-6}} = 2.23 \times 10^7\ \text{W/m}^2 = 2.23 \times 10^3\ \text{W/cm}^2 \tag{62}$$

Raster energy deposition. For a constant-speed raster, the linear energy density (energy delivered per unit track length) is:

$$E' = \frac{P_{\text{opt}}}{v} \tag{63}$$

With $v = 10\ \text{mm/s} = 0.01\ \text{m/s}$:

$$E' = \frac{70}{0.01} = 7000\ \text{J/m} = 7\ \text{J/mm} \tag{64}$$

If adjacent raster lines are spaced by s, the areal energy density (dose) is approximated as:

$$H = \frac{P_{\text{opt}}}{v\, s} \tag{65}$$

For a representative line spacing of $s = 1$ mm (50% overlap for a 2 mm spot):

$$H = \frac{70}{0.01 \times 0.001} = 7.0 \times 10^6 \text{ J/m}^2 = 700 \text{ J/cm}^2 \tag{66}$$

These relations show how commanded raster speed, line spacing/overlap, and power gating at turnarounds directly control thermal dose uniformity across a patch.

A.4 Lunar Night Survival Calculations

This section provides the governing relations for rover battery sizing during lunar night survival operations.

A.4.1 Survival Power Budget and Energy Requirement

The total rover survival load is the sum of the battery heater, electronics enclosure heater, and minimal wake-up avionics:

$$P_{\text{survival}} = P_{\text{batt,htr}} + P_{\text{enc,htr}} + P_{\text{avionics}} = 10 + 8 + 3 = 21 \text{ W} \tag{67}$$

The required battery energy capacity is:

$$E_{\text{batt}} = P_{\text{survival}} \times t_{\text{eclipse}} \times (1 + f_{\text{margin}}) \tag{68}$$

where t_{eclipse} is the site-specific worst-case eclipse duration determined in Phase F0 and f_{margin} is the design margin. Substituting baseline values of $t_{\text{eclipse}} = 96$ h and $f_{\text{margin}} = 0.25$:

$$E_{\text{batt}} = 21 \times 96 \times 1.25 = 2520 \text{ Wh} \approx 2.5 \text{ kWh} \tag{69}$$

A.4.2 Battery Mass Estimate

Battery pack mass is estimated from cell-level energy density and a usable depth of discharge limit:

$$m_{\text{batt}} = \frac{E_{\text{batt}}}{\rho_e \times \text{DoD}} \tag{70}$$

where $\rho_e \approx 200$ Wh/kg is the Li-ion cell energy density and DoD = 0.80 is the usable fraction. Plugging into the equation then gives:

$$m_{\text{batt}} = \frac{2520}{200 \times 0.80} = 15.75 \text{ kg} \tag{71}$$

This estimate represents cell mass only. Packaging, thermal interface materials, and battery management system (BMS) hardware will add mass at the system level, matching the 25% design margin already applied to the energy requirement.

A.5 Risk Matrix Details

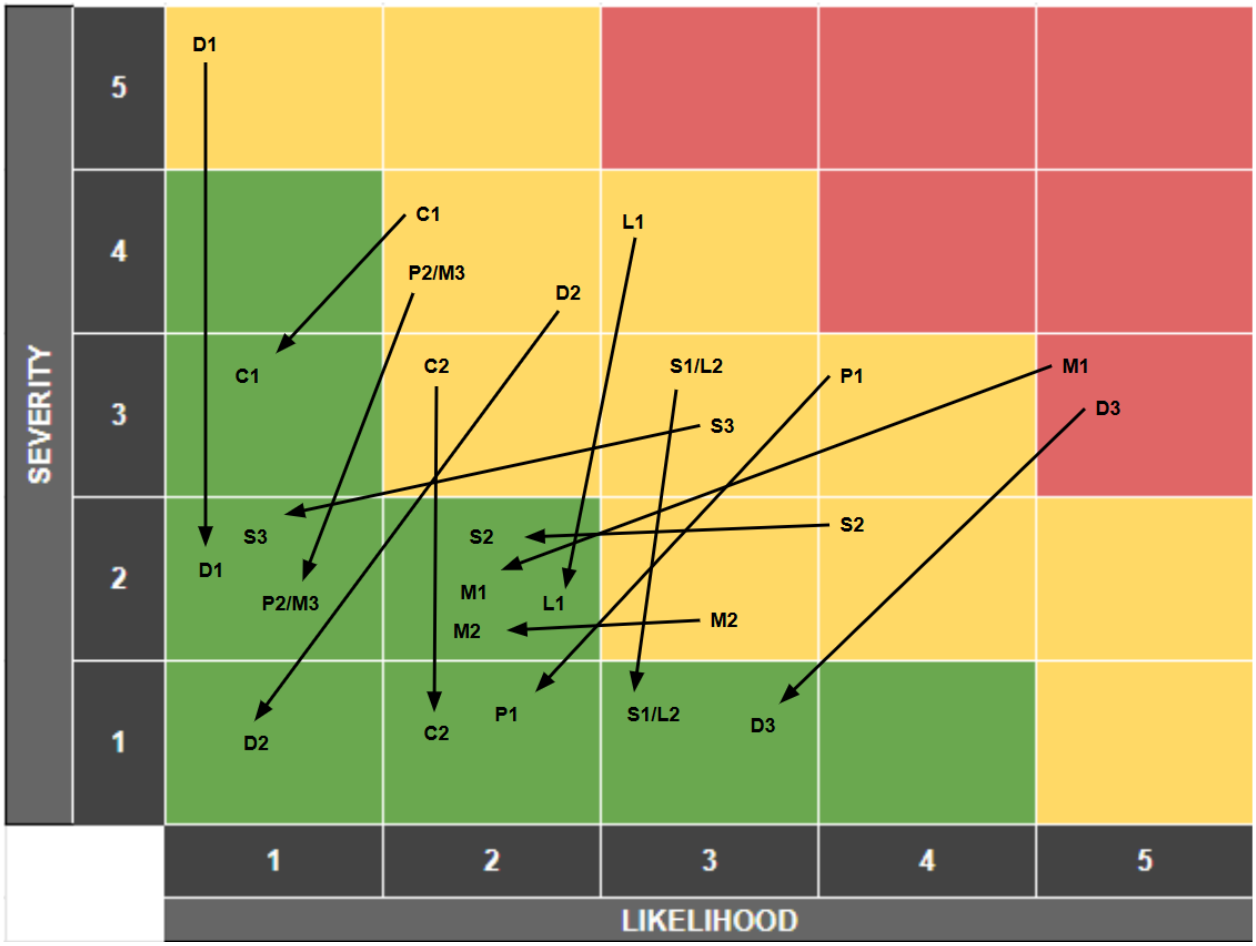

Position (start -> end)	Risk Description (very brief)	Mitigation Plan (more detailed)
C1 (4/2 -> 3/1)	Suspension motor malfunctions	Redundant wiring + error-catching program
C2 (3/2 -> 1/2)	Regolith kickup from overspin	Dust tolerant joints and instrument covers
S1 (3/3 -> 3/1)	Arm joints freeze up	Dry MoS2 lubricant (rated) + insulation + line heaters
S2 (2/4 -> 2/2)	Sunlight misses CPC	Heat sensor in CPC + onboard controller calc. focus axis intersect
S3 (4/3 -> 2/1)	Quartz rod overheats	Heat pipes + radiator panels on end compartment
L1 (4/3 -> 2/2)	Laser overheats	Heat pipes + radiator panels + power shutoff control
L2 (3/3 -> 3/1)	Arm joints freeze up	Dry MoS2 lubricant (rated) + insulation + line heaters
P1 (3/4 -> 1/2)	Dust contamination of sensor	Retractive covers + side walls to ensure dust travels vertically only
P2 (4/2 -> 2/1)	Nozzle lifts rover up	Pressure regulator + redundant mass from battery
M1 (3/5 -> 2/2)	Dust contamination test chamber	Motorized brush + electrostatic holder
M2 (3/2 -> 2/2)	Sintered pucks not picked up	Skip section of experiment
M3 (4/2 -> 2/1)	Erroneous readings from sensor	Redundant sensors + live transmission of data to verify
D1 (5/1 -> 2/1)	Rover ramp fails to deploy	Extensive testing in accordance with CLPS provider
D2 (4/2 -> 1/1)	Loss of communications	Redundant antennas + SSD memory to store data for low bps export
D3 (3/5 -> 1/3)	Plume kickup from initial landing	Arm is wrapped in scratch resistant insulation + mirrors/end effectors sealed via aperture covers

References

[1] G. Heiken, D. Vaniman, and B. French, *Lunar Sourcebook: A User's Guide to the Moon*. Cambridge, U.K.: Cambridge Univ. Press, 1991.

[2] W. D. Carrier, "Particle size distribution of lunar soil," *Journal of Geotechnical Engineering*, vol. 109, no. 3, pp. 273–284, 1983.

[3] J. K. Mitchell and W. N. Houston, "Soil mechanics evaluation of Apollo lunar rover performance," NASA TN D-8090, 1975.

[4] A. Colaprete et al., "The Volatiles Investigating Polar Exploration Rover (VIPER) mission," NASA Technical Report, 2021.

[5] E. Rezich et al., "Investigating the geotechnical properties of the lunar south pole with NASA VIPER's mobility system," *The Planetary Science Journal*, vol. 6, no. 169, 2025.

[6] VIPER Mobility Team, "Dust mitigation for the VIPER mobility system," NASA Technical Report, 2023.

[7] T. Nakamura and B. Smith, "Solar Thermal System for Lunar ISRU Applications: Development and Field Operation at Mauna Kea, HI," in *49th AIAA Aerospace Sciences Meeting*, AIAA 2011-433, Jan. 2011.

[8] J. Chaves, *Introduction to Nonimaging Optics*, 2nd ed. Boca Raton, FL: CRC Press, 2015.

[9] T. Nakamura, J. A. Case, and C. L. Senior, "Optical Waveguide Solar Energy System for Lunar Materials Processing," in *Engineering, Construction, and Operations in Space V*, pp. 783–790, 1996, doi: 10.1061/40177(207)106.

[10] Tempco Electric Heater Corporation, "Flexible Heater Design Guide," Wood Dale, IL, USA, 2017.

[11] AeroDIODE, "High Power Fiber-Coupled Laser Diodes Datasheet," 2020.

[12] FISBA AG, "Slow Axis Collimators (SAC) for Laser Diodes," White Paper, Aug. 2018.

[13] SemiNex Corporation, "Enhancing Laser Diode Output with Optical Lenses," Application Note, 2025.

[14] T. Thanadulsatit et al., "A review of structural and system design of Mars rover Curiosity and Perseverance," *Suranaree Journal of Science and Technology*, vol. 31, no. 2, 2024, doi: 10.55766/sujst-2024-02-e01241.

[15] S. J. Indyk and H. Benaroya, "A structural assessment of unrefined sintered lunar regolith simulant," *Acta Astronautica*, vol. 140, pp. 517–536, Nov. 2017, doi: 10.1016/j.actaastro.2017.09.018.

[16] Lunar and Planetary Institute, "Collecting Moon Rocks: Sample Collection Tools," Lunar Samples (Apollo), accessed Feb. 12, 2026.

[17] J. R. Gaier, K. Journey, S. Christopher, and S. Davis, "Evaluation of Brushing as a Lunar Dust Mitigation Strategy for Thermal Control Surfaces," in Proc. 41st International Conference on Environmental Systems (ICES), Portland, OR, USA, Jul. 17–21, 2011. NASA Technical Reports Server, Doc. ID 20110014222.

[18] E. McBryan, P. Francis, and A. Sobey, "Dust Mitigation for the VIPER Mobility System," in Proc. 54th International Conference on Environmental Systems (ICES), Prague, Czech Republic, Jul. 13–17, 2025. NASA Technical Reports Server, Doc. ID 20250005201.

[19] Z. S. Liu, A. S. Mahmud, K. G. Sjolund, et al., "Hybrid Dust Mitigation Brush Utilizing EDS and UV Technologies," Final Technical Paper, NASA BIG Idea Challenge, Georgia Institute of Technology, 2021.

[20] C. Soares, W. Hoey, A. Wong, and M. Grabe, "Plume-Induced Contamination Testing," Lunar and Planetary Science Conference (LPSC), 2020.

[21] J. Eberhart, R. West, and A. Korzun, "PFGT Data Overview — PFGT Tests at MSFC," NASA Technical Reports Server, 2021.

[22] Engineering ToolBox, "Nitrogen — Thermophysical Properties," n.d.

[23] G. P. Sutton and O. Biblarz, *Rocket Propulsion Elements*, 9th ed., John Wiley & Sons, 2016.

[24] Airgas, "Compressed Gas Cylinders — Tank Sizing Information (Technical Guide MCM-552)," n.d.

[25] D. A. Spencer, "Lunar South Pole Surface Temperatures," Lunar and Planetary Institute Conference Proceedings, 1995.

[26] European Space Agency (ESA), "GIADA 'Touches' the Comet! — Rosetta Mission Update," 2014.

[27] Astrobotic Technology, "Astrobotic Lunar Landers: Payload User's Guide," Ver. 5.02, Aug. 2021.

[28] B. Bluethmann et al., "VIPER Rover Overview and Mobility and Hardware," NASA Lunar Surface Innovation Consortium (LSIC), NASA Technical Reports Server, NTRS Doc. ID 20240013903, 2024.

[29] A. B. Morris, "Simulation of Rocket Plume Impingement and Dust Dispersal on the Lunar Surface," Ph.D. Dissertation, Dept. of Aerospace Engineering and Engineering Mechanics, The University of Texas at Austin, Austin, TX, 2012.

[30] Cryo Rocket, "5.2 Nozzle Geometry," *Cryo Rocket Flow Model*, [Online]. Available: https://www.cryo-rocket.com/flow-model/5.2-nozzle-geometry/. [Accessed: 14-May-2026].